Break in precipitation – temperature scaling over India predominantly explained by cloud-driven cooling

Sarosh Alam Ghausi[1,2], Subimal Ghosh[3,4] and Axel Kleidon[1]

[1] Biospheric Theory and Modelling Group, Max Planck Institute for Biogeochemistry, Jena 07745, Germany.
[2] International Max Planck Research School for Global Biogeochemical Cycles (IMPRS – gBGC), Jena 07745, Germany
[3] Department of Civil Engineering, Indian Institute of Technology Bombay 400076, India
[4] Interdisciplinary Programme in Climate Studies, Indian Institute of Technology Bombay 400076, India

Correspondence to: Sarosh Alam Ghausi (sghausi@bgc-jena.mpg.de)

Abstract. Climate models predict an intensification of precipitation extremes as a result of a warmer and moister atmosphere at the rate of 7%/K. However, observations in tropical regions show contrastingly negative precipitation-temperature scaling at temperatures above 23° - 25°C. We use observations from India and show that this negative scaling can be explained by the radiative effects of clouds on surface temperatures. Cloud radiative cooling during precipitation events make observed temperatures co-vary with precipitation, with wetter periods and heavier precipitation having a stronger cooling effect. We remove this confounding effect of clouds from temperatures using a surface energy balance approach constrained by thermodynamics. We then find a diametric change in precipitation scaling with rates becoming positive and coming closer to the Clausius – Clapeyron scaling rate (7%/K). Our findings imply that the intensification of precipitation extremes with warmer temperatures expected with global warming is consistent with observations from tropical regions when the radiative effect of clouds on surface temperatures and the resulting covariation with precipitation is accounted for.

1 Introduction

Climate models and observed trends have shown precipitation extremes to increase at the global scale with anthropogenic global warming (Fischer et al., 2013; Westra et al., 2013; Donat et al., 2016). This increase is largely explained by the thermodynamic Clausius-Clapeyron (CC) equation, suggesting a ≈7%/K increase in atmospheric moisture holding capacity per degree rise in temperature ("CC rate") (Allen & Ingram, 2002). Extreme precipitation is expected to increase at a similar rate (Trenberth et al., 2003; Held & Soden., 2006; O'Gorman & Schneider, 2009), as also shown by convection-permitting climate model projections (Kendon et al., 2014; Ban et al., 2015). Precipitation – temperature scaling rates, estimated using statistical methods and observed records, are widely used as an indicator to constrain this response (Lenderink et al., 2008; Wasko et al, 2014).

However, observed scaling rates show large heterogeneity globally, with significant deviations from the CC rate (Westra et al., 2014; Schroeer & Kirchengast, 2018). Deviations are larger in the tropical regions where scaling rates are mostly negative and precipitation extremes largely show a monotonic decrease or a sudden drop (hook) in scaling at high temperatures (Utsumi et al., 2011). These deviations have been studied and attributed to number of factors. Two primarily argued reasons include the moisture availability limitation at high temperatures (Hardwick et al., 2010) and dependence of scaling estimates on the wet event duration (Gao et al., 2018; Ghausi & Ghosh 2020; Visser et al., 2021). Cooling effects of rainfall events have also questioned the use of surface air temperature as scaling variable (Bao et al., 2017). Other scaling variables like atmospheric air temperature (Golroudbary et al., 2019), sampling temperatures before the start of storm (Visser et al., 2020), using measures of atmospheric moisture like dew point temperature (Bui et al., 2019) and integrated water vapor (Roderick et al., 2019) have been suggested as an alternative to surface air temperatures. The use of atmospheric moisture as a scaling variable has been criticized because it provides less insight about precipitation sensitivity to temperature and is also not entirely immune to cooling effects of rainfall (Bao et al., 2018). Other factors that can cause deviations in scaling includes the change in rainfall type from stratiform to convective (Berg et al., 2013; Molnar et al., 2015) and seasonality in precipitation (Sun et al., 2020). Owing to these uncertainties, the use of scaling relationships derived from observations to infer future changes in extreme precipitation in these regions remains debatable.

In this study, we show that a large part of uncertainties in this response and negative scaling rates in the tropics are mainly caused by the radiative effect of clouds on surface temperatures. Precipitation events are accompanied by strong cloud cover, which reduces the solar absorption at the surface and hence lowers surface temperatures. This radiative cooling associated with precipitation can be significant in the tropical regions where insolation and temperatures are high. As a result, regions and periods of more intense precipitation cool more, and this affects their position in the scaling curve. This implies that temperature observations are not independent of precipitation and this dependency obscures their scaling relationship. We used a thermodynamic systems approach to remove this cooling effect from surface temperatures. We then show that when this effect is being removed, no breakdown in the scaling relationship is seen in observations and extreme precipitation then scales positively with temperature close to CC rate.

To remove the effects of clouds, we used a surface energy balance formulation in conjunction with the first and second law of thermodynamics (Kleidon & Renner, 2013). This approach provides us with additional thermodynamic constraints on the turbulent flux exchange between surface and atmosphere. We used this thermodynamically constrained model and force it with the “all-sky” and “clear-sky” radiative fluxes. These fluxes are a standard product in NASA-CERES radiation datasets such that “all-sky” fluxes are representative of observed conditions including the cloud effects while “clear-sky” fluxes are diagnosed by removing the effect of clouds from the radiative transfer. Compounding the thermodynamic constraint on turbulent fluxes together with the radiative fluxes helps us to estimate “all-sky” and “clear-sky” temperatures that includes and excludes the radiative effects of clouds respectively.

We then evaluate this effect and its impact on precipitation-temperature scaling using observations from India. India is a tropical country where the extreme precipitation and the resulting floods have intensified over the past years (Goswami et al., 2006) and are expected to increase in the future (Katzenberger et al., 2021). However, extreme precipitation–temperature scaling is largely negative over most of India (Vittal et al., 2016; Sharma et al., 2019), which is in contrast to the observed trends (Roxy et al., 2017). In this study, we attempt to resolve this inconsistency in precipitation – temperature scaling by removing the cloud cooling effects from surface temperatures. To do this, we use gridded precipitation – temperature datasets that were used in previous studies (Vittal et al., 2016; Mukherjee et al., 2018; Sharma et al., 2019; Ghausi et al., 2020) and supplement it with the gridded radiative flux datasets to remove the cloud radiative effects. More details on our surface energy-balance model and estimation of surface temperatures "with" and "without" clouds are followed in the section 2.1 with the details of datasets being used in section 2.2. We used these reconstructed temperatures to study the effect of clouds on precipitation – temperature scaling over India. To estimate the precipitation – temperature scaling rates, we used the widely adopted statistical methods. Details of them are further provided in section 2.3. Results are then presented and discussed in section 3.

2 Methods and Data

2.1 Thermodynamically constrained energy balance model

To infer surface temperatures from the radiative forcing and remove the effects of clouds, we start with a simple physical formulation of the surface energy balance. The surface of the Earth is heated by solar absorption and downwelling longwave radiation. This heat is released back to the atmosphere through surface emission of longwave radiation and exchange of turbulent fluxes of sensible and latent heat. This balance between the incoming and outgoing energy fluxes at the Earth's surface is described by equation (1).

$$\boldsymbol{R_s + R_{l,down} = R_{l,up} + J} \qquad \textbf{(1)}$$

Here R_s is the surface net solar absorption, R_{ld} is the downwelling longwave radiation, $R_{l,up}$ is the upwelling longwave radiation emitted from the surface and J is turbulent flux exchange between surface and the atmosphere (comprising of sensible and latent heat). We neglect the ground heat flux, as it is generally small when averaged over a few days or longer. While R_s and $R_{l,down}$ can be obtained using radiation datasets for different sky conditions, the partitioning between $R_{l,up}$ and J is poorly constrained by surface energy balance alone. To have these additional constraints on J, we used a thermodynamic systems approach to view the earth system. Similar approach had also been used in (Kleidon & Renner, 2013; Kleidon et al., 2014; Dhara et al., 2016) and were found to very well capture the observed surface temperatures, energy partitioning and climate sensitivities.

To do this, we conceptualize the surface atmosphere system as a heat engine, with warm Earth surface as the heat source and cooler atmosphere being the sink (Figure 1). Heat and mass are transported within this engine by the exchange of turbulent fluxes (J) between the surface and the atmosphere. The differential radiative heating and cooling between the surface and the atmosphere maintains the temperature difference and drives the vertical convective motion. The power (G) associated with the work done by the heat engine required to sustain convective motion in form of vertical mixing and exchange of turbulent fluxes can be derived simply using the first and second law of thermodynamics and can be represented by the well-established Carnot limit as

$$\boldsymbol{G = J\left(1 - \frac{T_a}{T_s}\right).} \qquad \textbf{(2)}$$

Detailed derivation about this can be found in (Kleidon & Renner, 2013; Kleidon et al., 2014). Here T_a and T_s are the representative temperatures of cold atmosphere and the hot surface respectively. Both temperatures are inferred from their respective energy balances. The atmospheric temperature (T_a) is assumed to be equal to the radiative temperature of atmosphere (T_r) and is estimated using the outgoing longwave radiation at top of atmosphere ($R_{l,toa}$)

$$\boldsymbol{T_a = \left(\frac{R_{l,toa}}{\sigma}\right)^{1/4}} . \qquad \textbf{(3)}$$

Here, σ is the Stefan Boltzmann constant ($\sigma = 5.67 \times 10^{-8}$ $Wm^{-2}K^{-4}$). A correction of 15K was applied to the radiative temperature to account for the assumption of black atmosphere and effective height of convection (Dhara et al., 2016). We consider the atmosphere as opaque to terrestrial radiation and hence it is assumed that all outgoing longwave radiation emitted into space originates from the atmosphere.
The heat engine source temperature i.e. surface temperature (T_s) can be expressed from the emitted longwave radiation from the surface ($R_{l,up}$) as

$$\boldsymbol{T_s = \left(\frac{R_{l,up}}{\sigma}\right)^{1/4}}. \qquad \textbf{(4)}$$

Using the surface energy balance (Eq. 1), we can then express the surface temperature in terms of net solar absorption, downwelling longwave radiation and turbulent fluxes (J) as

$$\boldsymbol{T_s} = \left(\frac{\boldsymbol{R_s} + \boldsymbol{R_{l,down}} - \boldsymbol{J}}{\boldsymbol{\sigma}}\right)^{\mathbf{1/4}} . \qquad \textbf{(5)}$$

The differential radiative heating and cooling between the surface and the atmosphere maintains the temperature difference and drives the vertical convective motion. Thermodynamics sets a limit to this conversion and thus constrains the amount of turbulent flux exchange. Less turbulent fluxes result in a hotter surface (Eq. 5), which will increase the temperature difference between the surface and atmosphere. This will subsequently increase the efficiency term in the generation rate, the second term on the right-hand side of Eq. (2). On the other hand, an increase in turbulent fluxes (J) increases the first term in the generation rate of Eq. (2), but it will, in turn, reduce the surface temperature and temperature difference between surface and atmosphere (Eq. 5). Thus, there exists a trade-off that sets the limit for the power to maintain vertical energy and mass exchange between surface and the atmosphere. This limit is termed as the maximum power limit and provides an additional constraint to surface energy balance partitioning that we used here to infer surface temperatures.

Using Equations. (2), (3) and (5), the rate of work done (power) produced by the heat engine can be expressed as a function of turbulent fluxes (J) as

$$\boldsymbol{G} = \boldsymbol{J}\left(\mathbf{1} - \boldsymbol{T_a}\left(\frac{\boldsymbol{R_s} + \boldsymbol{R_{l,down}} - \boldsymbol{J}}{\boldsymbol{\sigma}}\right)^{\mathbf{-1/4}}\right). \qquad \textbf{(6)}$$

Note that power G = 0 when J = 0 or when J = R_s + $R_{l,down}$ - $R_{l,toa}$. Hence, there is a maximum G_{max} = G ($J_{maxpower}$) for a value between 0 < $J_{maxpower}$ < R_s + $R_{l,down}$ - $R_{l,toa}$. The optimum J that maximizes power was calculated numerically. This flux was then used to determine the surface temperatures.

$$\boldsymbol{T_{s,maxpower}} = \left(\frac{\boldsymbol{R_s} + \boldsymbol{R_{l,down}} - \boldsymbol{J_{maxpower}}}{\boldsymbol{\sigma}}\right)^{\mathbf{1/4}} \qquad \textbf{(7)}$$

Surface temperatures were estimated using Eq. 7 for “all-sky” and “clear-sky” radiative conditions using radiative forcing from the NASA – CERES datasets. We then refer to these two temperatures derived using Eq. 7 as “all-sky” and “clear-sky” temperatures.

2.2 Datasets used

Radiative fluxes of shortwave and longwave radiation at surface and top of atmosphere (TOA) were obtained from the NASA - CERES (EBAF 4.1) dataset (Loeb et al., 2018; Kato et al., 2018) and NASA CERES Syn1deg dataset (Doelling et al., 2013,2016). These datasets are available for both "all-sky" as well as "clear-sky" conditions at monthly and daily scale respectively with a 1° latitude x 1° longitude spatial grid resolution and were used as a forcing in our energy balance model. We evaluated our model using observations derived gridded temperature data from Indian Meteorological Department (IMD, Rajeevan et al., 2008). To estimate the precipitation – temperature scaling, we used daily gridded precipitation and temperature datasets with a spatial resolution of 1° latitude x 1° longitude from the Indian Meteorological Department (IMD, Rajeevan et al., 2008) and 3 hourly gridded rainfall data from NASA-TRMM_3B42 with a spatial resolution of 0.25° x 0.25°. We repeated the analysis using daily gridded precipitation and temperature data from the APHRODITE (Asian Precipitation Highly Resolved Observational Data Integration towards Evaluation) dataset, available at a spatial resolution of 0.25° x 0.25° (Yatagai et al., 2012). To further ensure robustness of our results, we also used 3 station-based daily precipitation – temperature observations in India (Mumbai Airport, Bangalore Airport and Chennai Airport) from global surface summary of the day (GSOD) data provided by National Oceanic and Atmospheric Administration (NOAA). Daily dew point temperatures were obtained from the ERA-5 reanalysis. Based on the availability of all datasets, the period of analysis was chosen from the years 2003 to 2015.

2.3 Estimation of precipitation – temperature scaling rates

Extreme precipitation events were scaled with observed, "all-sky" and "clear-sky" temperatures using two widely adopted scaling approaches: The Binning Method (Lenderink et al., 2008) and Quantile Regression (Wasko et al., 2014). For the binning method, we defined extreme precipitation events using a threshold of 99th percentile precipitation contained at each grid cell. Precipitation – temperature pairs were then divided into the increasing order of non-overlapping bins of 2 K width. Only those bins which have at least 150 data points have been considered for the analysis (Utsumi et al., 2011). The median value of each bin was then used to examine the variation of precipitation extremes with temperature. Bins with temperature less than 3°C were discarded to remove the effects of freezing, thawing and snowfall. To ensure that our results are not biased with the number of data points in each bin and bin sizes (which may affect the nature of the scaling relationship), we further used the Quantile Regression method to estimate the scaling rates.

Quantile regression estimates the conditional quantile of the dependent variable (in our case, precipitation) over the given values of the independent variable (temperature). We first fitted a quantile regression model between the logarithmic precipitation and temperature values at the target quantile of 99%

$$\boldsymbol{Log(P_i) = \beta_o^{99} + \beta_1^{99}(T_i)} \quad . \qquad (\mathbf{8})$$

Here P_i denotes the mean daily precipitation intensity and T_i is the daily mean temperature, and β_o^{99} and β_1^{99} are the regression coefficients for the 99th quantile of precipitation. The slope coefficient β_1^{99} is then exponentially transformed to estimate the scaling rate (α_1).

$$\boldsymbol{\alpha_1 = 100\,.\left(e^{\beta_1^{99}} - 1\right)} \qquad (\mathbf{9})$$

The forementioned methodology had been widely adopted to estimate the extreme precipitation – temperature scaling in previous studies (Lenderink et al., 2008, 2010; Utsumi et al., 2011; Wasko et al., 2014; Schroeer et al., 2018).

3 Results and Discussion

In this section, we first start by a quick evaluation of our thermodynamic approach by comparing the estimated “all-sky” temperatures against observations. We then quantify the cloud radiative effects on surface temperatures and check for its spatial consistency across regions. We then estimated precipitation – temperature scaling rates by including and excluding the effect of clouds on surface temperatures. We also used dew point temperature (a proxy measure for atmospheric moisture) as a scaling variable. Later, we discuss our interpretation of scaling by excluding cloud effects from temperatures, its comparison with the dew point scaling and its implications across regions.

3.1: Evaluating the modelled temperatures

"All-sky" temperatures were estimated using the daily observed radiative fluxes from CERES in conjunction with surface energy partitioning constrained by maximum power (see Equation 7). We found an extremely good agreement of these estimated temperatures when compared to surface temperature observations over India with $R^2 > 0.9$ and RMSE < 1.5 K over most regions (Figure 2). This signifies that our formulation strongly captures the surface temperature variation over India and thus validates our approach. We then extend this for clear-sky conditions by forcing our model with "clear-sky" radiative fluxes from CERES and estimating "clear-sky" temperatures. It is to note that "clear-sky" temperatures are reconstructed temperatures estimated by removing the effect of clouds from radiative transfer.

3.2: Estimating the cloud radiative cooling

We used the difference between the "all-sky" and "clear-sky" temperatures as a measure to quantify the effect of cloud-driven cooling during rainfall events. This cooling increases strongly with precipitation across regions, resulting in a stronger reduction in surface temperature with greater precipitation (Figure 3a). This cooling is predominantly caused by the substantial reduction in absorbed solar radiation at the surface for "all-sky" conditions compared to "clear-sky" conditions (Figure 3b). On the other hand, changes in longwave radiation are comparatively small and largely remain insensitive to precipitation.

To examine the spatial consistency in precipitation variability and associated cooling, we isolated extreme daily precipitation days over each grid. Figure 4a shows the mean magnitude of daily extreme precipitation events over India. The pattern was consistent with the cloud cover map from NASA-CERES (shown in Appendix C). Figure 4b shows the cloud-cooling associated with these days. This cooling effect of clouds and precipitation shows a clear, systematic variation across India. The cooling effect is greater where precipitation rates are high. In contrast, in the more arid regions in the northwest of India, the cooling effect almost disappears with low precipitation rates. In the Northernmost Himalayan region, the difference in "clear-sky" and "all-sky" temperatures is negative. These high-altitude regions are more sensitive to changes in longwave radiations. As a result, there is a significant increase in longwave radiation with increase in cloud cover which compensates for the cooling due to reduction in shortwave over those grids. Figure 4c further shows the mean "all-sky" temperature during these days. We find that the heaviest events occur at a relatively lower temperature as a result of stronger cooling. Figure 4d shows the mean number of rainfall days per year. More rainy days implies more cloudy conditions and thus a stronger cloud radiative cooling over that region. Having quantified this effect of cloud radiative cooling and its systematic variation across regions, we then estimate its impact on the precipitation – temperature scaling.

3.3 Impact on precipitation-temperature scaling

We performed a binning analysis (Lenderink et al., 2008) to understand the scaling of precipitation extremes with temperature using observed temperatures as well as our estimated "clear-sky" and "all-sky" temperatures. Precipitation events were isolated and binned into P-T pairs and the resulting scaling relationships are shown in Figure 5. The scaling relationship using observed and "all-sky" temperatures showed similar scaling behaviour (yellow and red lines in Figure 5a). Extreme precipitation increases close to the CC rate up to a threshold of around 23° - 24°C, above which the scaling becomes negative. This break in scaling behaviour with observed temperatures is consistent with the findings of previous studies (Hardwick et al., 2010; Ghausi & Ghosh, 2020) and is commonly referred in literature as “hook" or “peak structure" (Wang et al., 2017; Gao et al., 2018). However, when precipitation extremes are scaled with "clear-sky" temperatures that excludes the cloud-cooling effect, the resulting scaling relationship does not show a breakdown and increases consistently, close to the CC rate over the whole temperature range (blue line in Fig. 5a). Similar results were obtained when the scaling curves were reproduced for station-based observations (See Appendix A).

Previous studies (Hardwick et al., 2010; Chan et al., 2015; Wang et al., 2017) have attributed the break in precipitation-temperature scaling to a lack of moisture availability as relative humidity tends to decrease at high temperatures. To account for this effect of moisture limitation, some studies used dew point temperature, a measure of atmospheric humidity, as an alternative scaling variable (Wasko et al., 2018; Barbero et al., 2018). They showed that the breakdown and negative scaling disappear when scaled with dew point temperatures (Zhang et al., 2019; Ali et al., 2021). To evaluate this interpretation and compare it to ours, we used the dew point temperature from the ERA-5 reanalysis. We derived the extreme precipitation scaling using this temperature (Figure 5b) and compared it to our "all-sky" and "clear-sky" temperatures (Figure 5c).

At first sight, the scaling relationship using dew point temperatures looks very similar to our "clear-sky" relationship (compare Figures 5a and 5b, but note the difference in temperature scale). Yet, its interpretation differs because using dew point temperatures merely implies that the intensity of extreme precipitation events scales with the moisture content of the air, with moister air resulting in higher intensity events. Dew point scaling thus carries less insight about the response of extreme precipitation to climate warming (Bao et al., 2018). To infer the precipitation sensitivity with temperature from dew point scaling, one then needs to see how dew point temperatures change with actual temperatures (dT_{dew}/dT) (Figure 5c). This is further demonstrated using equation 10.

$$\frac{dP}{dT} = \frac{dP}{dT_{dew}} \times \frac{dT_{dew}}{dT} \qquad \textbf{(10)}$$

If relative humidity remains unchanged, we would expect the dew point temperature to increase continuously with surface temperature, representing a moisture increase of 7%/K. However, when dew point temperatures are compared to "all-sky" temperatures (red line, Figure 5c), we note that a break occurs in this scaling as well. Dew point temperatures increase with "all-sky" temperatures for colder temperatures more strongly than what would be expected from an unchanged relative humidity when air gets warmer. However, at temperatures of above 23° - 25°C, dew point temperatures fall, reflecting a decrease in relative humidity that is typical for warm, arid regions. Thus, one does not see a breakdown in precipitation - dew point scaling because the information on the breakdown is contained in how dew point temperatures change with surface air temperatures (second term in equation 10). Similar findings were also reported in Roderick et al (2019).

The scaling of dew point temperatures with "clear-sky" temperatures is much more uniform and consistent across the whole temperature range and does not show a breakdown or a super CC scaling in the relationship. This is because the "clear-sky" temperatures reflect the radiative conditions, and not the effects of atmospheric humidity or clouds. In contrast, observed temperatures and "all-sky" temperatures co-vary with cloud effects, which in turn are linked to precipitation and humidity, thus resulting in less clear scaling relationships that are less straightforward to interpret. This further implies that moisture loading of the atmosphere primarily occurs during the non-precipitating periods that are more representative of clear-sky radiative conditions.

The breakdown in scaling effect can thus be explained by the cooler temperatures associated with precipitation events. This cooling shifts the precipitation extremes to lower temperature bins while the high-temperature bins then correspond to more arid regions or to the drier pre-monsoon season temperatures with lower values of precipitation extremes. We refer to this as a “bin-shifting” effect. The cooling effect is proportional to the amount of precipitation (Fig. 3A) and hence, the heavier the precipitation, the stronger the cooling and bin shifting becomes. When the cloud cooling effect is removed, as in the case of "clear-sky" temperatures, extreme precipitation then shows a scaling that is consistent with the CC rate. This bin shifting effect arising due to the presence of clouds also causes a decrease in relative humidity at higher temperatures. This effect can be seen by the stronger increase in dewpoint temperatures below 25°C, and the decline above this temperature (Figure 5c). The breakdown in scaling is thus not directly related to changes in aridity or moisture availability, but rather to the radiative effect of clouds on surface temperature.

To demonstrate the implications of our interpretation for precipitation scaling across regions, we estimated regression slopes of 99th percentile precipitation events for both sub-daily (TRMM) and daily (IMD & APHRODITE) precipitation with the different temperatures using the Quantile Regression method (Wasko et al., 2014). We found that extreme precipitation scaling was negative for both, observed and "all-sky" temperatures over most regions (Figure 6) except for the Himalayan foothills in the North of India. The scaling rates for sub-daily extremes were slightly higher than those estimated for daily extremes but yet remains negative over most grids. When the cooling effect of clouds is removed by using "clear-sky" temperatures, extreme precipitation scaling then shows a diametric change and scaling estimates come close to CC rates over most of the regions. A similar diametric change in the scaling was also obtained with the APHRODITE precipitation dataset (Appendix B). The highest positive sensitivities were found over the Central Indian region where a widespread increase in rainfall extremes is already reported (Roxy et al., 2017). There seems to be a minor difference between the clear sky scaling in IMD and TRMM in foothill of Himalayas north of India, which is likely because of the underestimation of rainfall by TRMM over this region (Sharma et al., 2020; Shukla et al., 2019).

We also note that negative scaling was found over few regions of South-central and south-east India with “clear-sky” temperatures at both daily and sub-daily scales (Figure 6 c,f). To our understanding, this negative scaling primarily arises due to two reasons. Firstly, these are the grids which receives contribution from rainfall during both summer and winter monsoon, However, a relatively higher proportion of the rain happens during winter monsoon (Figure C1). The reason being that this region lies over the leeward side of Western ghats for the incoming southwest monsoon winds during summer monsoon. Whereas during the winter monsoon, Northeast winds blow over Bay of Bengal leading to large moisture advection and more rain over this region. As a result of this seasonality effect more extreme precipitation are sampled during winter season over this region while during the summer season, moisture supply may limit these extremes to increase. This may lead to a negative scaling when a single quantile regression slope is fitted over the whole temperature range. Another reason could be the development of low-pressure system in Bay of Bengal during winter months which causes cyclones over the Eastern coast of India. These cyclonic systems cause very high rainfall at very low temperatures which can lead to negative scaling (Traxl et al., 2021). More work is needed to be done to resolve these systems in conventional scaling approach and remains an important area for future research.

The effect of seasonality on precipitation scaling was also checked by producing the scaling curves for different seasonal subsets (summer and winter monsoon). We find a change in scaling during summer season after removing the cloud effects as the drop disappears (See Appendix C). Winter season on the other hand is associated with reduced rainfall amounts (less than 20%) and less clouds over most regions resulting in a similar scaling for both “all-sky” and “clear-sky” temperatures.

While there exist some differences, cloud cooling effect largely explains the negative scaling over most of the grid points over India. Extreme precipitation increases monotonically with temperature when the cloud cooling effect is removed. This implies that the “peak-structures” obtained with observed scaling will not constrain the rise in extremes with anthropogenic warming. The confounding effect between precipitation and temperature on observed scaling relationships, also termed as “apparent scaling” had also been argued by some recent studies (Bao et al. 2017; Visser et al., 2020). Our results agree with these studies that the observed scaling relationships also reflect the impact of synoptic conditions and cooling associated with precipitation events on temperature. However, we suggest that this confounding effect is largely associated with cloud radiative effect, which is removed by our use of “clear-sky” temperatures as a scaling variable. We also address the arguments raised to resolve apparent scaling using dew point temperature (Barbero et al., 2018). Our results confirm that precipitation extremes scale well with dew point temperatures as a measure for atmospheric moisture, but that the break in scaling actually originates from the scaling of dew point temperatures with observed temperatures. This response of dew point temperature to warming is further affected by the presence of clouds and associated radiative cooling. "Clear-sky" temperatures are independent of the co-variations arising from cloud effects and are thus a better, more independent measure and scaling variable to understand the precipitation response to climate warming.

4 Summary and Conclusions

We showed that the observed negative scaling of extreme precipitation in India arises mostly from the cloud radiative cooling of surface temperatures. When this effect is removed, we get a positive scaling consistent with the CC rate. Scaling rates estimated from observed temperatures are thus likely to misrepresent the response of extreme precipitation to global warming, because the cooling effects of clouds make precipitation and temperature covary with each other. When this effect is removed by estimating surface temperatures for "clear-sky" conditions, the scaling relationships with moisture content and precipitation become much clearer and confirm the CC scaling of extreme precipitation events with warmer temperatures. This explains the apparent discrepancy between the observed negative scaling rates over India and the projected increase in precipitation extremes by climate models.

While the scaling with “clear-sky” temperatures shows a diametric change and significant improvement over observed scaling, there still exist regional variabilities in scaling rates and deviations from CC scaling (7%/K). We believe that these deviations could be due to the following reasons. Firstly, present scaling approach does not explicitly consider the contribution from the large-scale dynamics and regional circulation patterns which can cause local changes in the scaling estimates. The effect of change in rainfall types - Orographic, stratiform or convective is not accounted for and it can affect the estimates of scaling rates. Lastly, Inconsistencies between precipitation and radiation datasets can also cause uncertainties in estimating the cooling associated with rainfall event and can affect the estimates of scaling rates.

It is also important to note that the goal of our study was not to compare the accuracy of scaling estimates from different gridded and station-based datasets, but rather to identify and remove the physical effects that causes uncertainties in this response. Our methodology to remove the cooling effect of clouds from surface temperatures significantly improves the scaling estimate for daily precipitation scaling. While our study was confined over the Indian region, we would expect that cloud effects on surface temperatures can explain the deviations in precipitation scaling from CC rates in other tropical regions too. Furthermore, our methodology to remove the cloud cooling effects on surface temperatures could be extended to derive scaling relationships of other, observed variables to obtain their response to global warming as well. Our findings add a novel component to better interpret precipitation scaling rates derived from observations to support climate model projections.

Data Availability

The daily gridded precipitation and temperature datasets were obtained from the Indian Meteorological department (IMD, https://cdsp.imdpune.gov.in/home_gridded_data.php (doi: 10.1029/2008GL035143). The APHRODITE (Asian Precipitation Highly Resolved Observational Data Integration towards Evaluation) dataset is available at http://aphrodite.st.hirosaki-u.ac.jp/products.html. Sub-daily precipitation data at 3 hourly resolution was obtained from TRMM (Tropical Rainfall measuring mission) TMPA_3B42_V7 data (doi: 10.5067/TRMM/TMPA/3H/7) https://disc.gsfc.nasa.gov/datasets/TRMM_3B42_7/summary. Station-based daily precipitation - temperature data was taken from NOAA – GSOD sites (Station id: 43295099999, 43003099999 and 43279099999) at https://www.ncei.noaa.gov/access/search/data-search/global-summay-of-the-day. Surface and TOA gridded radiative flux datasets are obtained from NASA CERES EBAF data (doi: https://doi.org/10.5067/Terra-Aqua/CERES/EBAF_L3B.004.1) and NASA CERES Syn1deg data (doi: 10.5067/TERRA+AQUA/CERES/SYN1DEG-1HOUR_L3.004A) at https://ceres.larc.nasa.gov/data/. Daily dew point temperature data is obtained from the ERA-5 reanalysis (doi: 10.24381/cds.e2161bac).

Acknowledgements

The author thanks the NASA CERES team for making the satellite data openly available (doi: 10.5067/Terra-Aqua/CERES/EBAF_L3B.004.1 and 10.5067/TERRA+AQUA/CERES/SYN1DEG-

1HOUR_L3.004A) and the Copernicus Climate Change Service for the access to the ERA-5 reanalysis data (doi: 10.24381/cds.e2161bac).

Author Contribution

All the authors contributed to the idea and development of the hypothesis. SAG carried out the data analysis. The writing of the manuscript was done by SAG with inputs and edits from AK. AK and SG helped in designing the study. All the authors contributed to the interpretation of the results.

References

1. Acero, F., García, J., & Gallego, M. (2011). Peaks-over-Threshold Study of Trends in Extreme Rainfall over the Iberian Peninsula. Journal of Climate, 24(4), 1089-1105. Retrieved May 31, 2021, from http://www.jstor.org/stable/26190418
2. Ali, H., Fowler, H. J., Lenderink, G., Lewis, E., & Pritchard, D. (2021). Consistent large-scale response of hourly extreme precipitation to temperature variation over land. Geophysical Research Letters, 48, e2020GL090317. https://doi.org/10.1029/2020GL090317
3. Allen, M., Ingram, W. Constraints on future changes in climate and the hydrologic cycle. Nature 419, 228–232 (2002). https://doi.org/10.1038/nature01092
4. Ban,N.,J .Schmidli, and C.Schär(2015), Heavy precipitation in a changing climate: Does short-term summer precipitation increase faster?, Geophys. Res. Lett., 42, 1165–1172, doi:10.1002/2014GL062588.
5. Bao, J., Sherwood, S. C., Alexander, L. V. & Evans, J. P. Comments on "temperature-extreme precipitation scaling: A two-way causality?". Int. J. Climatol. 38, 4661–4663 (2018).
6. Bao, J., Sherwood, S., Alexander, L. et al. Future increases in extreme precipitation exceed observed scaling rates. Nature Clim Change 7, 128–132 (2017). https://doi.org/10.1038/nclimate3201
7. Barbero, R., Westra, S., Lenderink, G. & Fowler, H. J. Temperature-extreme precipitation scaling: a two-way causality? Int. J. Climatol. 38, e1274–e1279 (2018).

8. Berg, P., Moseley, C., & Haerter, J. O. (2013). Strong increase in convective precipitation in response to higher temperatures. Nature Geoscience, 6(3), 181–185. https://doi.org/10.1038/ngeo1731
9. Bui A, Johnson F and Wasko C 2019 The relationship of atmospheric air temperature and dew point temperature to extreme rainfall Environ. Res. Lett. 14 074025
10. Chan, S.C., Kendon, E.J., Roberts, N.M., Fowler, H.J. and Blenkinsop, S. (2015) Downturn in scaling of UK extreme rainfall with temperature for future hottest days. Nature Geoscience, 9(1), 24– 28. https://doi.org/10.1038/ngeo2596.
11. Dhara, C., Renner, M., & Kleidon, A. (2016). Broad climatological variation of surface energy balance partitioning across land and ocean predicted from the maximum power limit. https://doi.org/10.1002/2016GL070323.1.
12. Doelling DR, Loeb NG, Keyes DF, Nordeen ML, Morstad D, Nguyen C, Sun M (2013) Geostationary enhanced temporal interpolation for CERES flux products. J Atmos Oceanic Technol 30(6):1072–1090
13. Doelling DR, Sun M, Nguyen LT, Nordeen ML, Haney CO, Keyes DF, Mlynczak PE (2016) Advances in geostationary-derived longwave fluxes for the CERES synoptic (SYN1 deg) product. J Atmos Oceanic Technol 33(3):503–521
14. Donat, M. G., Lowry, A. L., Alexander, L. V., O'Gorman, P. A. & Maher, N. More extreme precipitation in the world's dry and wet regions. Nat. Clim. Change 6, 508–513 (2016)
15. Fischer, E. M., Beyerle, U. & Knutti, R. Robust spatially aggregated projections of climate extremes. Nat. Clim. Change 3, 1033–1038 (2013).
16. Gao, X., Zhu, Q., Yang, Z., Liu, J., Wang, H., Shao, W., & Huang, G. (2018). Temperature Dependence of Hourly, Daily, and Event-based Precipitation Extremes Over China. Scientific Reports, 8(1), 1–10. https://doi.org/10.1038/s41598-018-35405-4
17. Ghausi, S. A., & Ghosh, S. (2020). Diametrically Opposite Scaling of Extreme Precipitation and Stream flow to Temperature in South and Central Asia, 1–10. https://doi.org/10.1029/2020GL089386

18. Golroudbary, V. R., Zeng, Y., Mannaerts, C. M., & Su, Z. (2019). Response of extreme precipitation to urbanization over the Netherlands. Journal of Applied Meteorology and Climatology, 58(4), 645–661. https://doi.org/10.1175/jamc-d-18-0180.1
19. Goswami, B. N., Venugopal, V., Sengupta, D., Madhusoodanan, M. S. & Xavier, P. K. (2006). Increasing trend of extreme rain events over India in a warming environment. Science 314, 1442–5. DOI: 10.1126/science.1132027
20. Hardwick Jones, R., Westra, S., & Sharma, A. (2010). Observed relationships between extreme sub-daily precipitation, surface temperature, and relative humidity. Geophysical Research Letters, 37(22), 1–5. https://doi.org/10.1029/2010GL045081
21. Held, I. M. and Soden, B. J.: Robust responses of the hydrological cycle to global warming, J. Climate, 19, 5686–5699, 2006.
22. Kato, S., F. G. Rose, D. A. Rutan, T. E. Thorsen, N. G. Loeb, D. R. Doelling, X. Huang, W. L. Smith, W. Su, and S.-H. Ham, 2018: Surface irradiances of Edition 4.0 Clouds and the Earth's Radiant Energy System (CERES) Energy Balanced and Filled (EBAF) data product, J. Climate, 31, 4501-4527, doi:10.1175/JCLI-D-17-0523.1
23. Katzenberger, A.; Schewe, J.; Pongratz, J.; Levermann, A. Robust increase of Indian monsoon rainfall and its variability under future warming in CMIP-6 models. Earth Syst. Dyn. 2020.
24. Kendon, E. J., Roberts, N. M., Fowler, H. J., Roberts, M. J., Chan, S. C., & Senior, C. A. (2014). Heavier summer downpours with climate change revealed by weather forecast resolution model. Nature Climate Change, 4(7), 570–576. https://doi.org/10.1038/nclimate2258
25. Kleidon, A., & Renner, M. (2013). A simple explanation for the sensitivity of the hydrologic cycle to climate change. Earth System Dynamics, 4(2), 455–465. https://doi.org/10.5194/esd-4-455-2013
26. Kleidon, A., Renner, M., & Porada, P. (2014). Estimates of the climatological land surface energy and water balance derived from maximum convective power. Hydrology and Earth System Sciences, 18, 2201–2218. https://doi.org/10.5194/hess-18-2201-2014

27. Lenderink, G., & Van Meijgaard, E. (2008). Increase in hourly precipitation extremes beyond expectations from temperature changes. Nature Geoscience, 1(8), 511–514. https://doi.org/10.1038/ngeo262
28. Loeb, N. G., Doelling, D. R., Wang, H., Su, W., Nguyen, C., Corbett, J. G., Liang, L., Mitrescu, C., Rose, F. G., and Kato, S.: Clouds and the Earth's Radiant Energy System (CERES) Energy Balanced and Filled (EBAF) Top-of-Atmosphere (TOA) Edition-4.0 data product, J. Climate, 31, 895–918, https://doi.org/10.1175/JCLI-D-17-0208.1, 2018.
29. Molnar, P., Fatichi, S., Gaál, L., Szolgay, J., & Burlando, P. (2015). Storm type effects on super Clausius-Clapeyron scaling of intense rainstorm properties with air temperature. Hydrology and Earth System Sciences, 19(4), 1753–1766. https://doi.org/10.5194/hess-19-1753-2015
30. Mukherjee S, Saran A, Stone D, Mishra V (2018) Increase in extreme precipitation events under anthropogenic warming in India. Weather Clim Extrem 20:45–53. https://doi.org/10.1016/j.wace.2018.03.005
31. O'Gorman, P. A. & Schneider, T. The physical basis for increases in precipitation extremes in simulations of 21st-century climate change. Proc. Natl Acad. Sci. USA 106, 14773–14777 (2009).
32. Rajeevan, M., Jyoti Bhate, A.K.Jaswal : Analysis of variability and trends of extreme rainfall events over India using 104 years of gridded daily rainfall data., , 2008, Geophysical Research Letters, Vol.35, L18707, doi:10.1029/2008GL035143.
33. Roderick TP, Wasko C, Sharma A. 2019Atmospheric moisture measurements explain increases in tropical rainfall extremes. Geophys. Res. Lett. 46, 1375–1382. (doi:10.1029/2018GL080833)
34. Roxy, M. K., Ghosh, S., Pathak, A., Athulya, R., Mujumdar, M., Murtugudde, R., … Rajeevan, M. (2017). A threefold rise in widespread extreme rain events over central India. Nature Communications, 8(1), 1–11. https://doi.org/10.1038/s41467-017-00744-9

35. Schroeer, K., & Kirchengast, G. (2018). Sensitivity of extreme precipitation to temperature: the variability of scaling factors from a regional to local perspective. Climate Dynamics, 50(11), 3981–3994. https://doi.org/10.1007/s00382-017-3857-9

36. Sharma, S., & Mujumdar, P. P. (2019). On the relationship of daily rainfall extremes and local mean temperature. Journal of Hydrology, 572(September 2018), 179–191. https://doi.org/10.1016/j.jhydrol.2019.02.048

37. Sharma, S., Khadka, N., Hamal, K., Shrestha, D., Talchabhadel, R., & Chen, Y. (2020). How accurately can satellite products (TMPA and IMERG) detect precipitation patterns, extremities, and drought across the Nepalese Himalaya?. *Earth and Space Science*, *7*, e2020EA001315. https://doi.org/ 10.1029/2020EA001315

38. Shukla AK, Ojha CSP, Singh RP, Pal L, Fu D. Evaluation of TRMM Precipitation Dataset over Himalayan Catchment: The Upper Ganga Basin, India. *Water*. 2019; 11(3):613. https://doi.org/10.3390/w11030613

39. Sun, Q., Zwiers, F., Zhang, X. & Li, G. A comparison of intra-annual and long-term trend scaling of extreme precipitation with temperature in a large-ensemble regional climate simulation. J. Clim. 33, 9233–9245 (2020).

40. Traxl, D., Boers, N., Rheinwalt, A. *et al.* The role of cyclonic activity in tropical temperature-rainfall scaling. *Nat Commun* **12,** 6732 (2021). https://doi.org/10.1038/s41467-021-27111-z

41. Trenberth, K. E., Dai, A., Rasmussen, R. M., & Parsons, D. B. (2003). The changing character of precipitation. Bulletin of the American Meteorological Society, 84(9), 1205–1217+1161. https://doi.org/10.1175/BAMS-84-9-1205

42. Utsumi, N., Seto, S., Kanae, S., Maeda, E. E., & Oki, T. (2011). Does higher surface temperature intensify extreme precipitation? 38(June), 1–5. https://doi.org/10.1029/2011GL048426

43. Visser, J. B., Wasko, C., Sharma, A., & Nathan, R. (2020). Resolving Inconsistencies in Extreme Precipitation-Temperature Sensitivities. Geophysical Research Letters, 47(18), e2020GL089723. https://doi.org/10.1029/2020GL089723

44. Visser, Johan B., Conrad Wasko, Ashish Sharma, and Rory Nathan. " Eliminating the “Hook” in Precipitation–Temperature Scaling", Journal of Climate 34, 23 (2021): 9535-9549, accessed Nov 10, 2021, https://doi.org/10.1175/JCLI-D-21-0292.1
45. Vittal, H., Ghosh, S., Karmakar, S. et al. Lack of Dependence of Indian Summer Monsoon Rainfall Extremes on Temperature: An Observational Evidence. Sci Rep 6, 31039 (2016). https://doi.org/10.1038/srep31039
46. Wang, G., Wang, D., Trenberth, K. et al. The peak structure and future changes of the relationships between extreme precipitation and temperature. Nature Clim Change 7, 268–274 (2017). https://doi.org/10.1038/nclimate3239
47. Wasko, C., & Sharma, A. (2014). Quantile regression for investigating scaling of extreme precipitation with temperature. Water Resources Research, 50(4), 3608–3614. https://doi.org/10.1002/2013WR015194
48. Wasko, C., Lu, W. T., & Mehrotra, R. (2018). Relationship of extreme precipitation, dry-bulb temperature, and dew point temperature across Australia. Environmental Research Letters, 13(7). https://doi.org/10.1088/1748-9326/aad135
49. Westra, S., Alexander, L. V., & Zwiers, F. W. (2013). Global increasing trends in annual maximum daily precipitation. Journal of Climate, 26(11), 3904–3918. https://doi.org/10.1175/JCLI-D-12-00502.1
50. Westra, S., Fowler, H. J., Evans, J. P., Alexander, L. V., Berg, P., Johnson, F., et al. (2014). Future changes to the intensity and frequency of short-duration extreme rainfall. Rev. Geophys. 52, 522–555. doi: 10.1002/2014RG000464
51. Yatagai, A., Kamiguchi, K., Arakawa, O., Hamada, A., Yasutomi, N., & Kitoh, A. (2012). Aphrodite constructing a long-term daily gridded precipitation dataset for Asia based on a dense network of rain gauges. Bulletin of the American Meteorological Society, 93(9), 1401–1415. https://doi.org/10.1175/BAMS-D-11-00122.1
52. Zhang, W., Villarini, G., & Wehner, M. (2019). Contrasting the responses of extreme precipitation to changes in surface air and dew point temperatures. Climatic Change, 154(1–2), 257–271. https://doi.org/10.1007/s10584-019-02415-8

Figures:

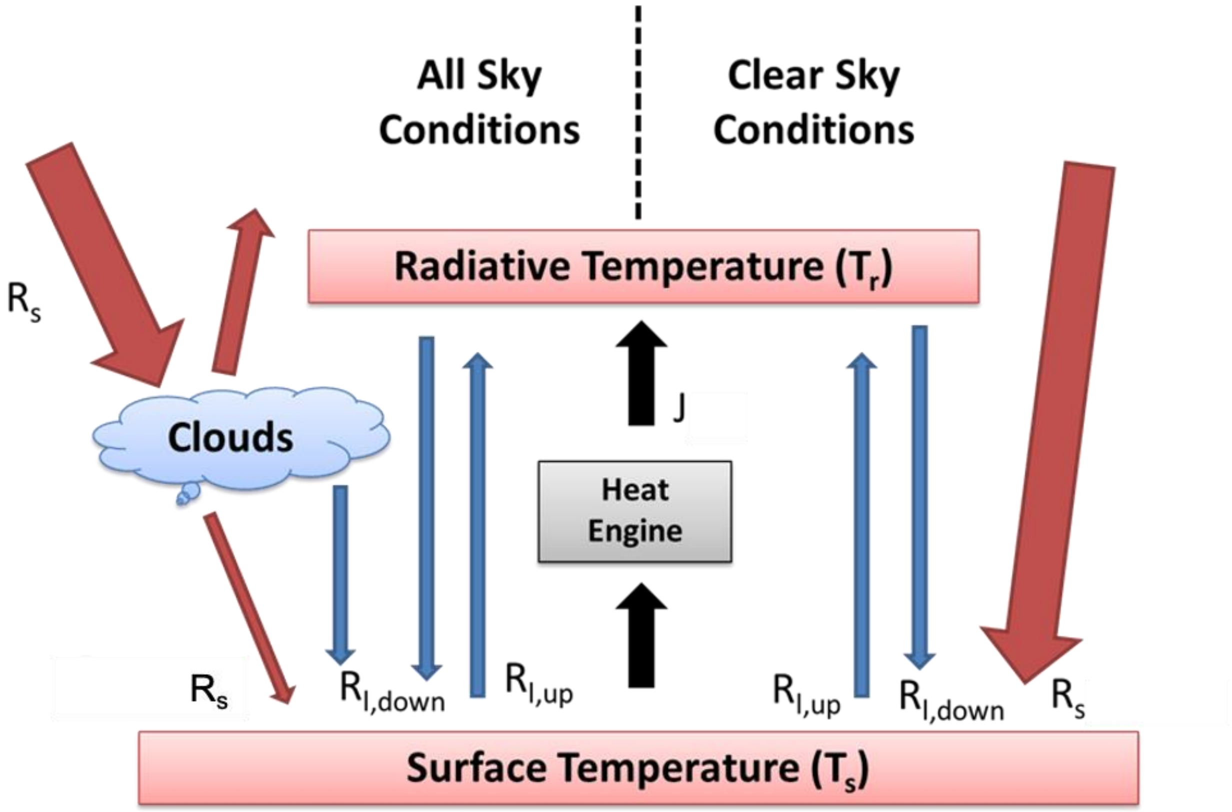

Figure 1. Schematic diagram of the surface energy balance, the fluxes of solar (red) and terrestrial (blue) radiation, as well as the turbulent heat fluxes (black). We consider turbulent heat exchange being driven primarily by an atmospheric heat engine that operates at the thermodynamic limit of maximum power.

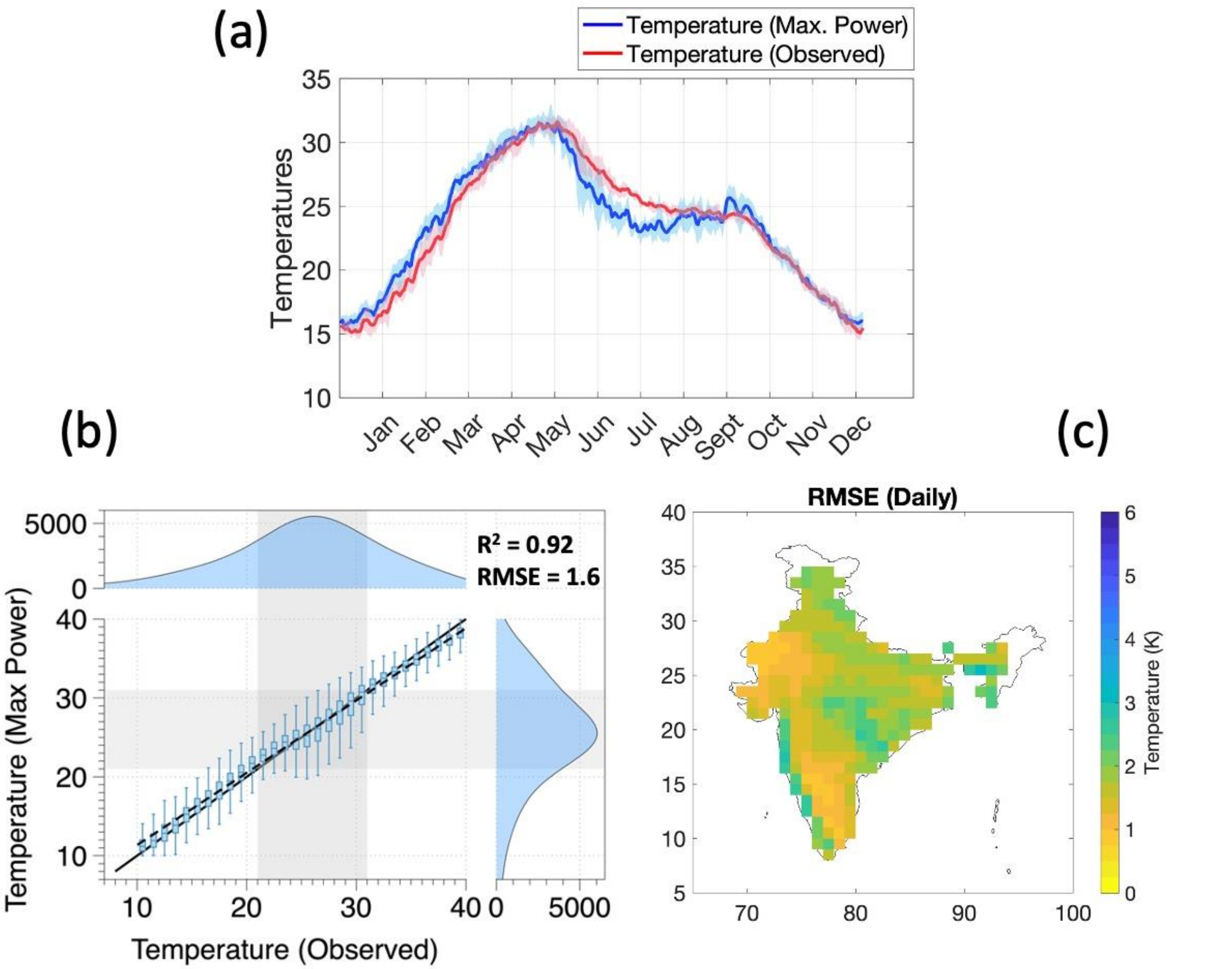

Figure 2: Comparison of daily annual cycle of temperature for observed (IMD) and estimated "all-sky" surface temperatures, averaged over all grid points. (B) Regression between the two temperatures at the grid-point scale. (C) Spatial variation of the root mean squared error (RMSE) in temperature estimates from maximum power compared to observed temperatures.

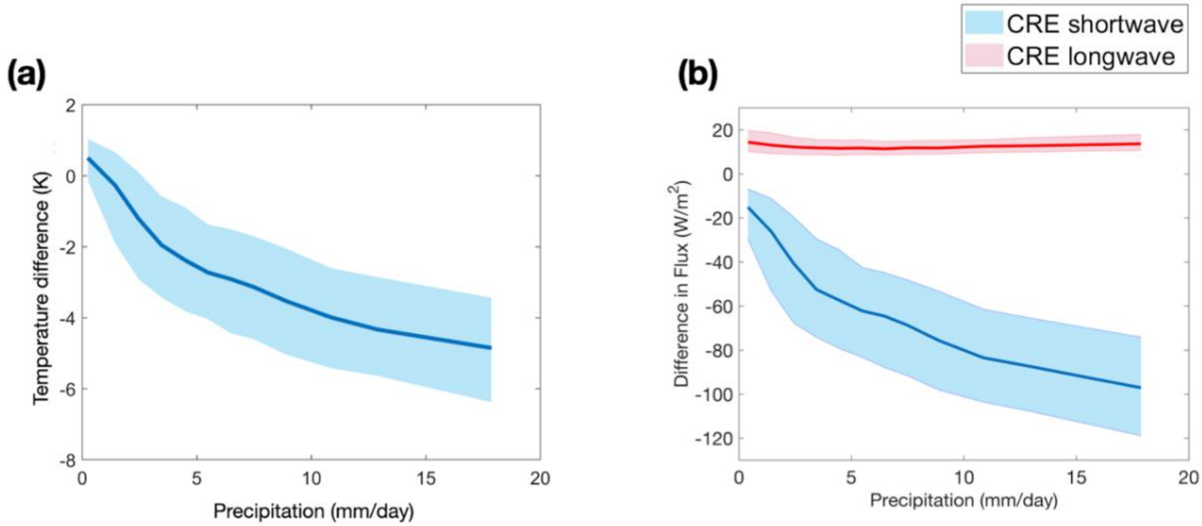

Figure 3: (a) Cooling effect of clouds on surface temperatures calculated from the difference of "all-sky" to "clear-sky" surface temperatures as a function of precipitation over the Indian region. (b) Difference in net shortwave and downwelling longwave radiative fluxes ("Cloud Radiative Effect", CRE) between "all-sky" and "clear-sky" radiative conditions at the surface as a function of precipitation. This was inferred using NASA – CERES (EBAF ed4.1) dataset (Loeb et al., 2018).

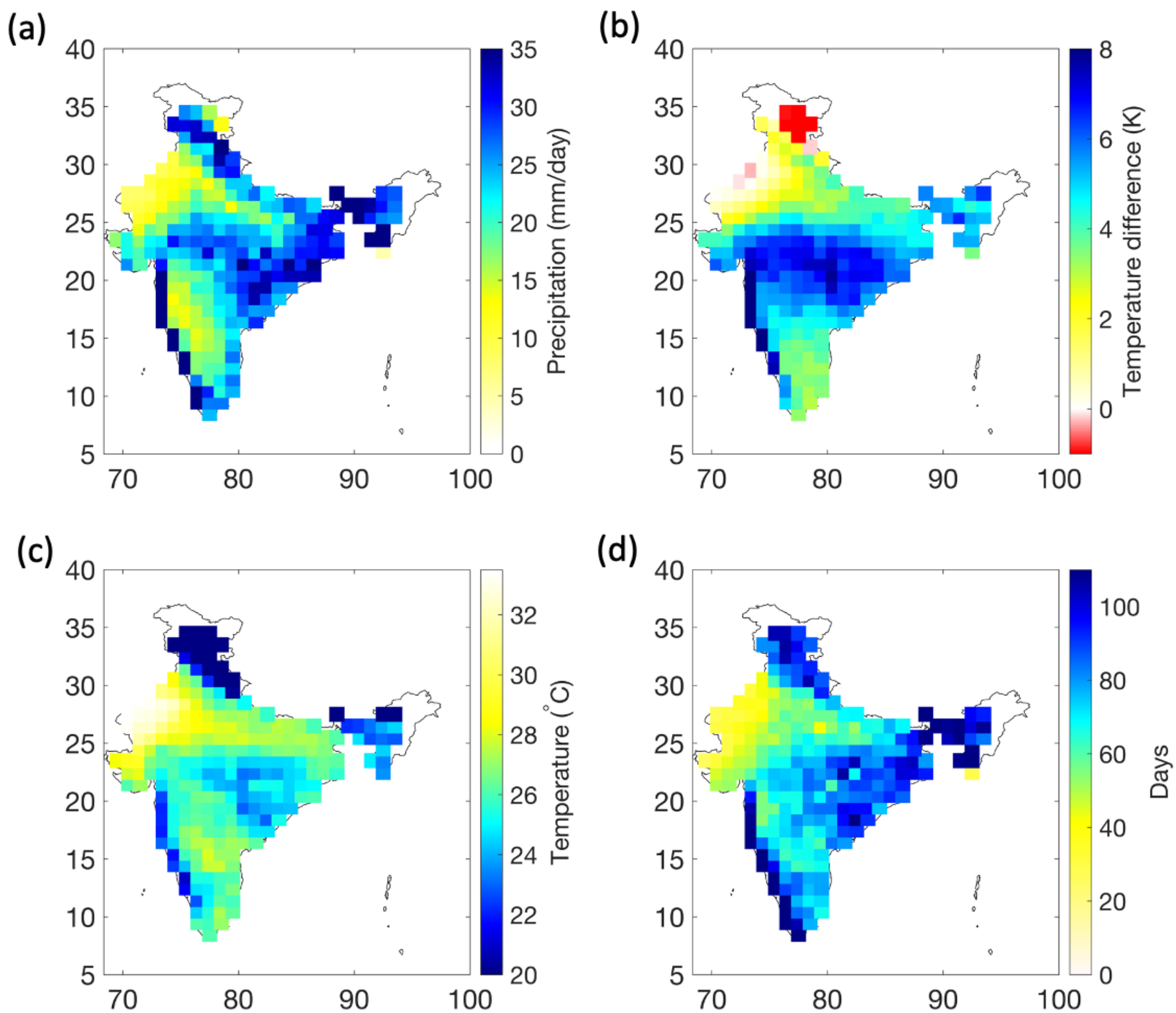

Figure 4. Regional variation of (a) mean daily extreme precipitation (99th percentile) (b) the temperature difference between "clear-sky" and "all-sky" radiative conditions averaged during extreme precipitation events (c) "All-sky" surface temperature during the occurrence of the event (d) Mean number of rainfall days per year

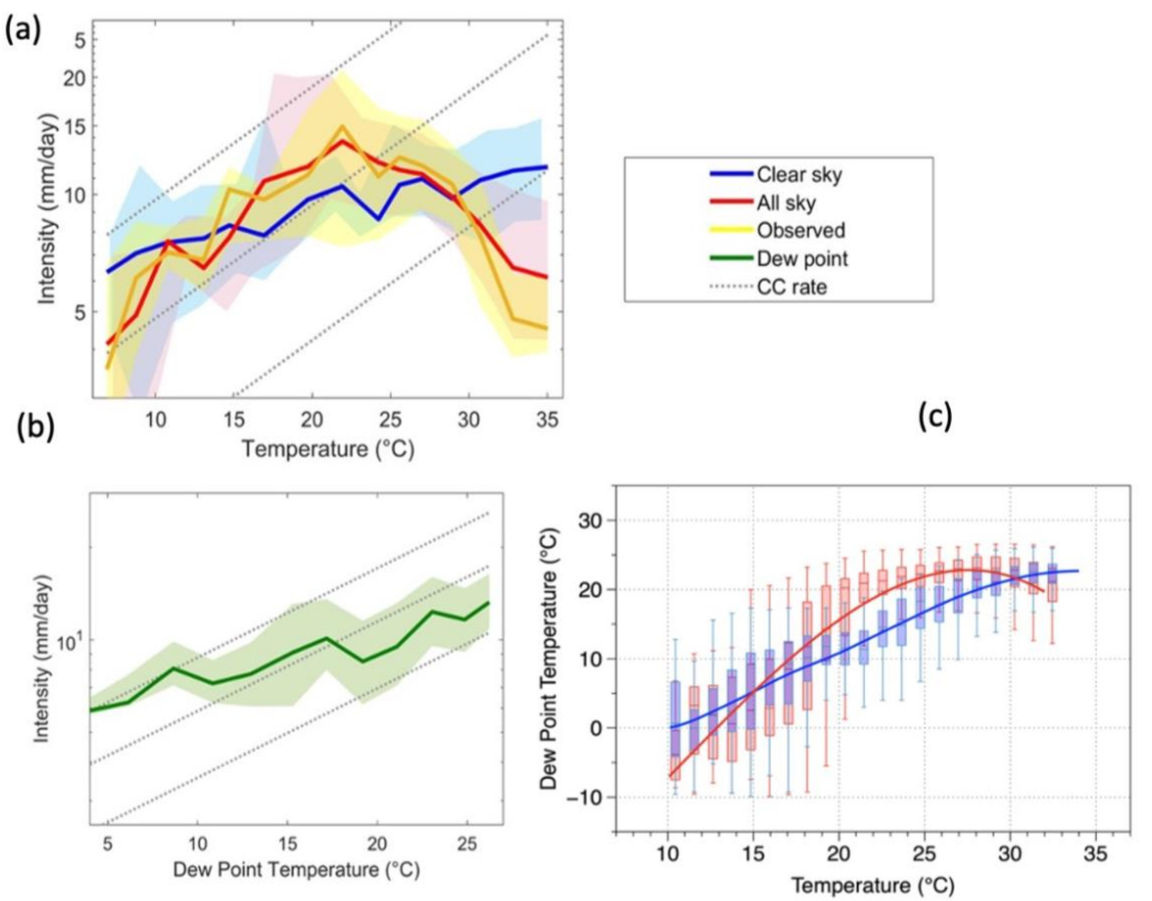

Figure 5. (a) Extreme precipitation-temperature scaling using observed (yellow), "all-sky" (red) and "clear-sky" (blue) temperatures over India. (b) Same as (a), but using dew point temperatures. (c) Relationship between dew point temperatures and "all-sky" (red) and "clear-sky" (blue) temperatures. The shaded areas represent the variance in terms of the interquartile range for each bin. Grey dotted lines indicate the Clausius-Clapeyron scaling rate. Note: Logarithmic vertical axis for figure (a,b)

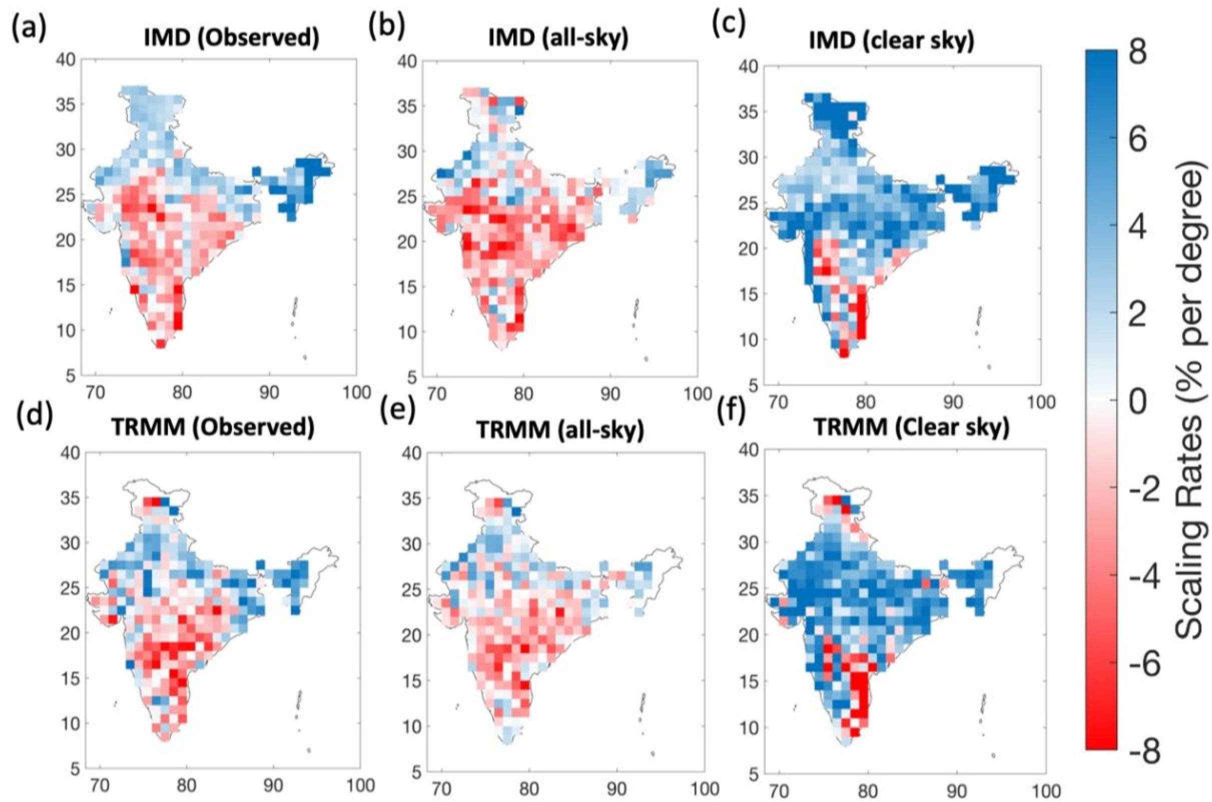

Figure 6. Regional variation of 99th percentile precipitation-temperature scaling rates using daily (a-c) and 3 hourly (d -f) rainfall data with observed temperatures (a, d), "all-sky" temperatures (b, e) and "clear-sky" temperatures (c, f).

Appendix A: Validation of scaling results using station-based GSOD data

We used three station-based daily observations from global surface summary of the day (GSOD) data provided by National Oceanic and Atmospheric Administration (NOAA). We used the data at Mumbai, Chennai and Bangalore Airport to produce the scaling curves (Appendix A). The choice of the station was based to ensure the robustness of results using gauge data as well as to check the effect of seasonality as the three sites receive rainfall during different period of the years. In Mumbai, rainfall occurs mainly during the summer monsoon season while in Chennai heavy rainfall occurs during the winter months (November and December). On other hand, Bangalore receives rainfall during both summer and winter monsoon season (Fig. A1 – row 1). Negative scaling was found over these three stations using observed (yellow) and “all-sky” (red) temperatures while with “clear-sky” temperatures (blue), we find positive rates largely consistent with the CC rate.

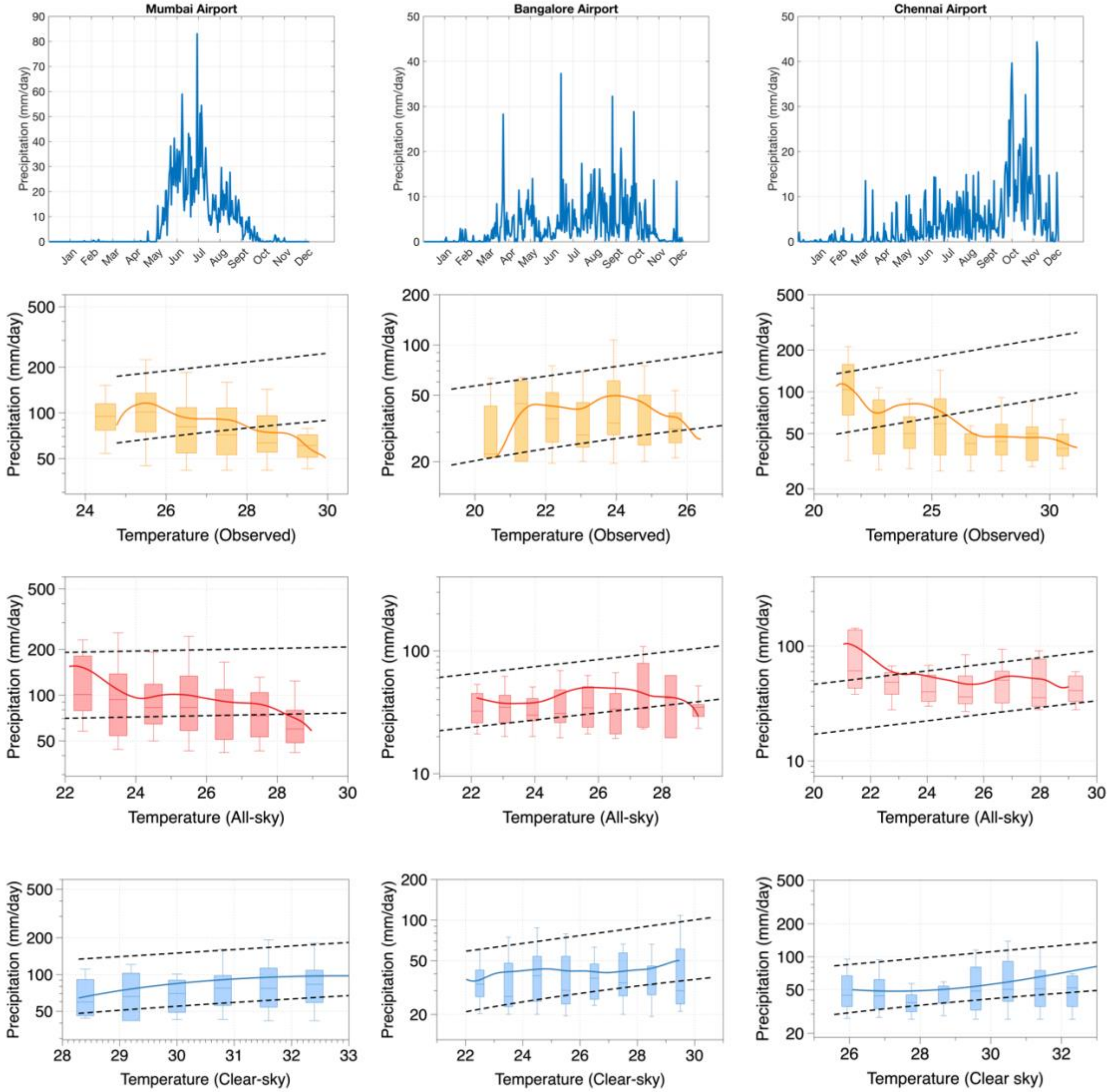

Figure A1. (Row 1) shows the annual cycle of mean daily precipitation over GSOD sites in Mumbai airport, Bangalore airport and Chennai airport respectively. Extreme precipitation – temperature scaling curves for observed temperatures (yellow), "all-sky" temperatures (red) and "Clear-sky" temperatures (in blue) are presented for all the three sites. Yellow/Red/Blue solid lines indicate the LOESS regression lines. Grey dotted lines indicate the Clausius-Clapeyron scaling rate. Note Logarithmic vertical axis.

Appendix B: Validation of scaling results using APHRODITE dataset

Figure B1 shows the spatial variation of daily precipitation – temperature scaling rates estimated from quantile regression (similar to Fig. 6 in the main text) using the APHRODITE (Asian Precipitation – Highly Resolved Observational Data Integration towards Evaluation of water resources) dataset (Yatagai et al., 2012). The results show a diametric change in scaling from being negative for observed and "all-sky" temperatures to coming close to CC rate (7%/K) for "clear-sky" temperatures. The findings were consistent with that obtained using the IMD and TRMM dataset (Figure 6).

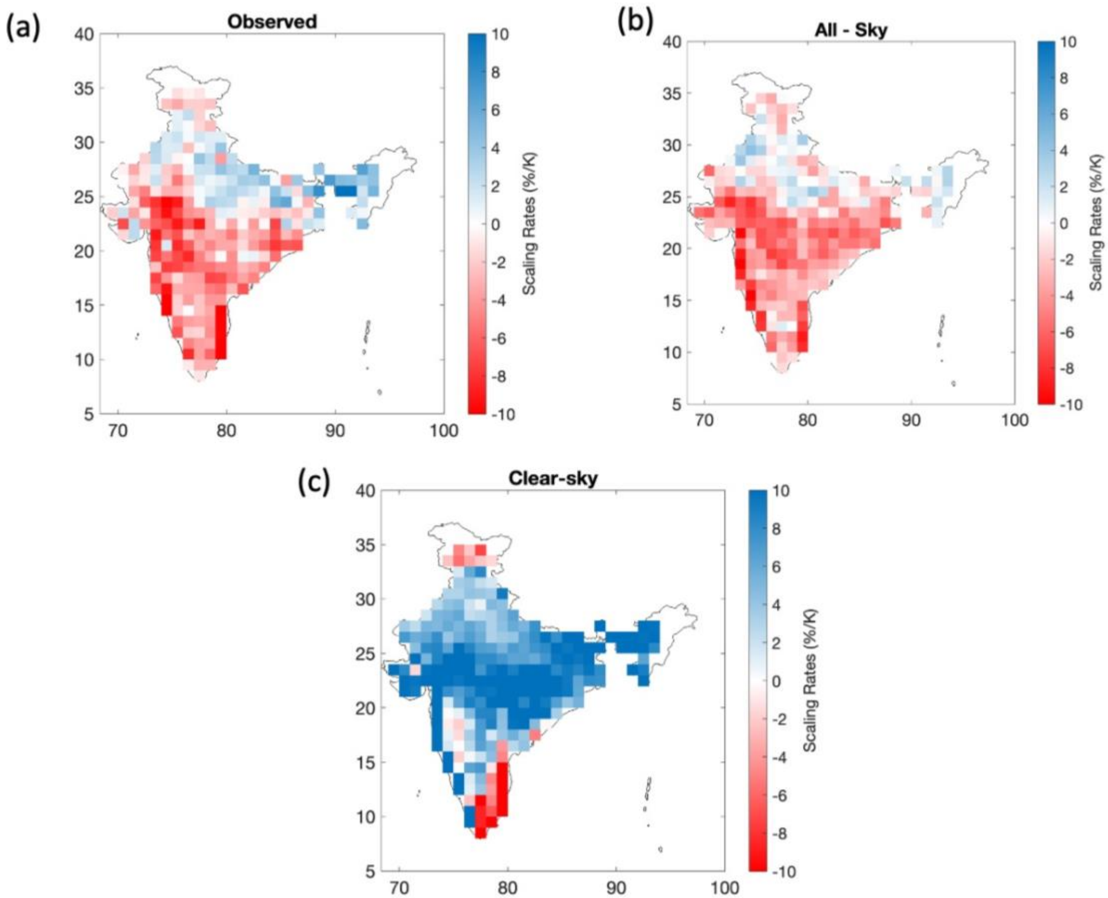

Figure B1. Regional variation of 99th percentile daily precipitation-temperature scaling rates using (a) Observed (b) "all-sky" and (c) "clear-sky" temperatures. Note: Precipitation data is from APHRODITE

Appendix C: Effect of seasonality on scaling rates

To understand the role of seasonality on precipitation – temperature scaling. We divided the precipitation period into two seasonal subsets i.e., summer monsoon season (April to September) and winter monsoon (October to March). Season wise scaling curves (estimated using LOESS regression) are presented in figure C3. We find that observed scaling is uniformly negative in summer over Indian region while during winter the scaling is positive (Fig C3-a, d). This is not surprising because the "hook" or breakdown in scaling happens at high temperature which leads to negative scaling in summer (Figure 5a). Reconstructed "All-sky" temperature showed scaling pattern consistent with observations (Fig. C3- b,e). When scaled with "clear-sky" temperatures, we observed a change in scaling for summer as it turns positive and come close to CC rate. While for winter the scaling does not change for "clear-sky" temperatures. It is also important to note that almost 80% of total rainfall over India occurs during the summer monsoon season (Fig C1). As a result, the cooling effect of clouds is mainly experienced during the summer monsoon (where we observed a change in scaling) while the cooling effect remains less than 1K during the winter season (Fig C2). Thus, one does not see a change in scaling between "all-sky" and "clear-sky" conditions for winter season.

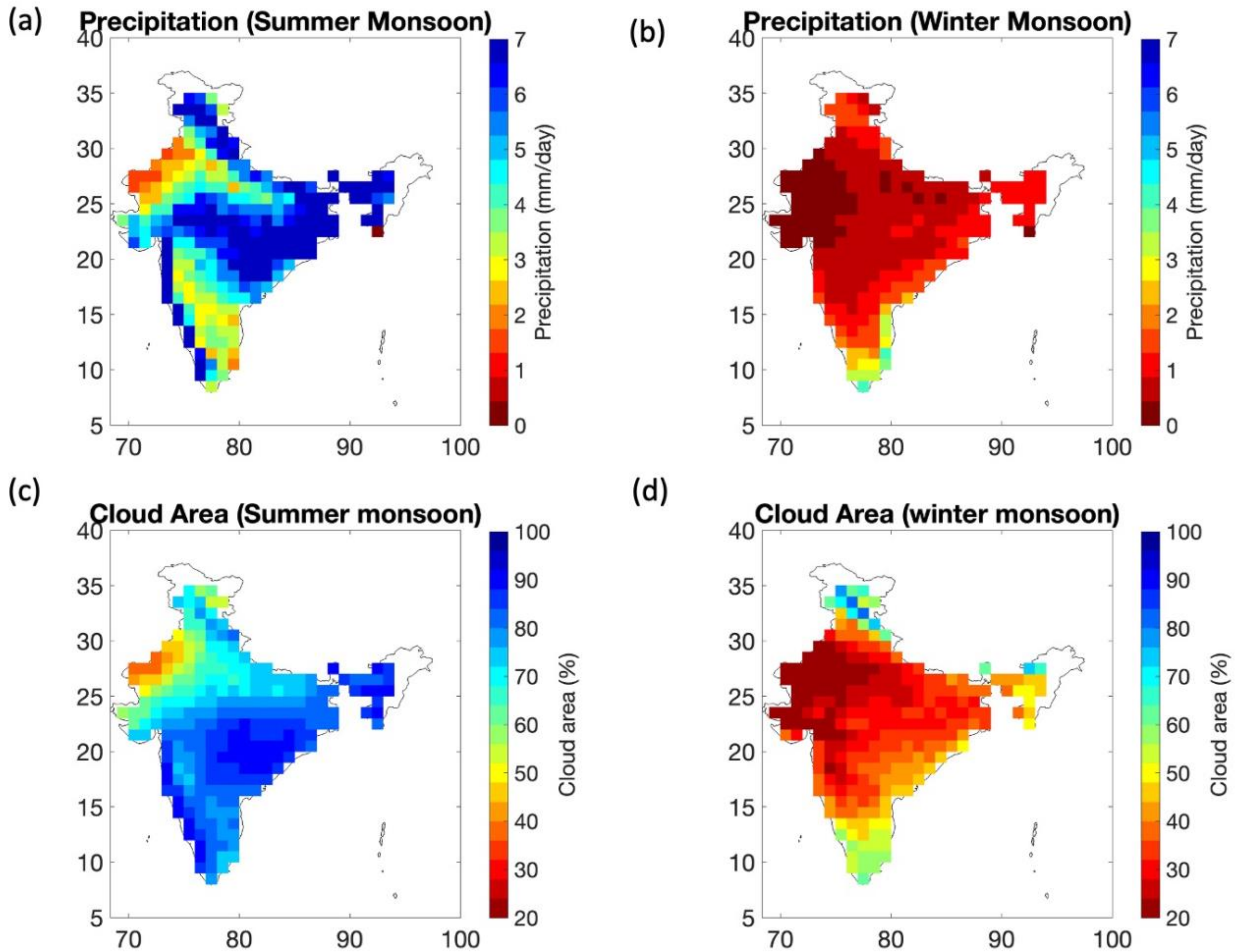

Figure C1. shows the map of mean daily precipitation (from IMD) and cloud area fraction (from NASA-CERES) during (a,c) summer monsoon (April – September) and during (b,d) winter monsoon (October – March).

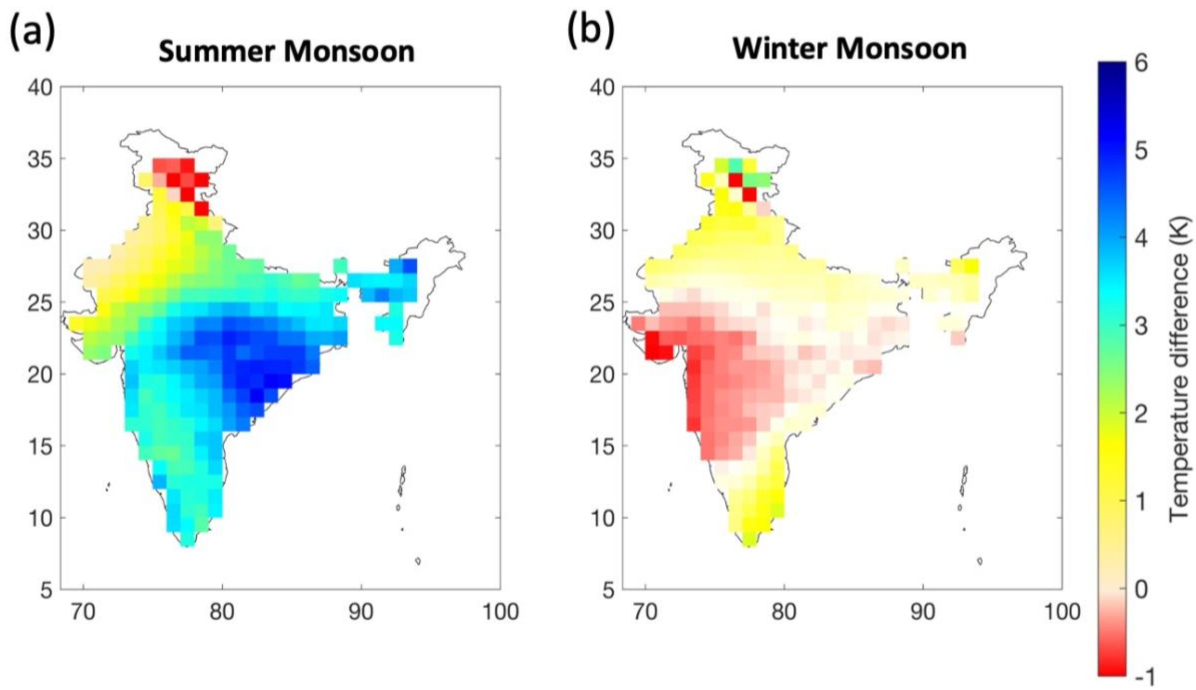

Figure C2. Shows the map of cooling of surface due to clouds (defined as the difference between "clear-sky" and "all-sky" temperatures) for (a) Summer monsoon (April – September) and (b) Winter monsoon (October – March)

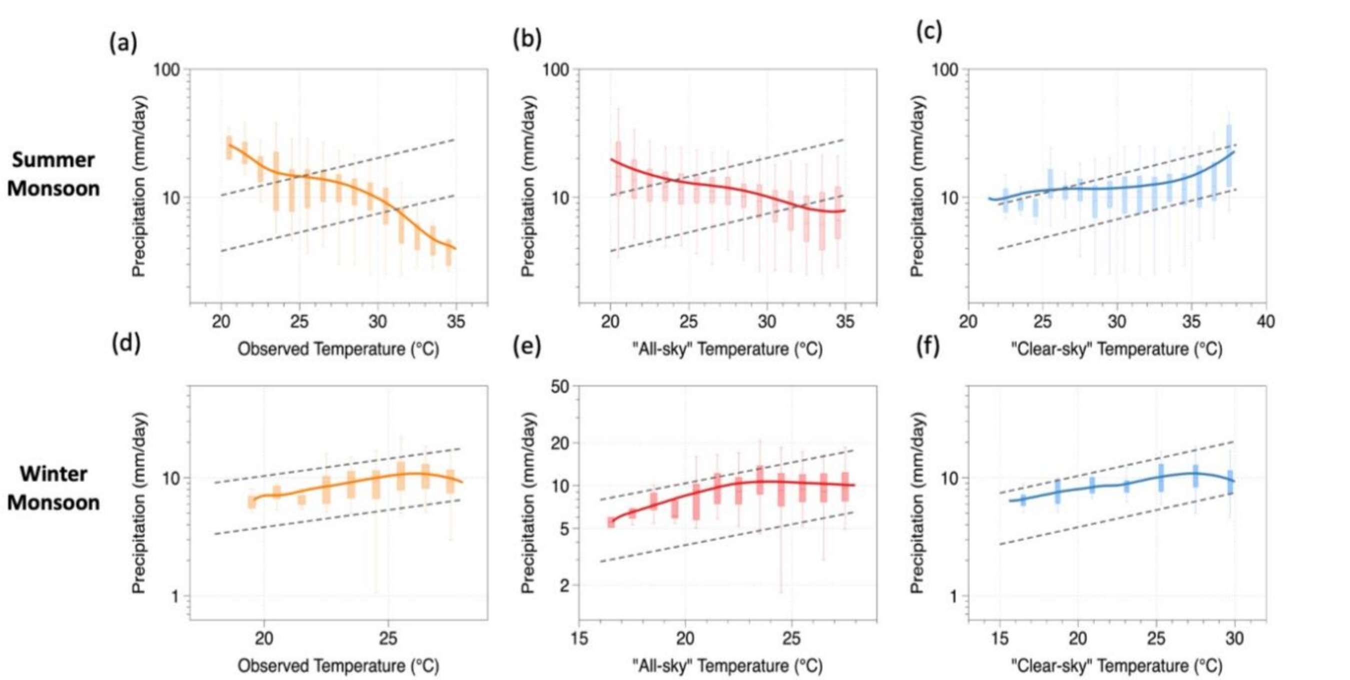

Figure C3. Extreme precipitation - temperature scaling during summer monsoon (a - c) and winter monsoon (d-f). Scaling curves are shown in yellow (a,d) for observed temperatures, in red (b,e) for "all-sky" temperatures and in blue (c,f) for "clear-sky" temperatures. Yellow/red/blue solid lines indicate the LOESS regression lines. Grey dotted lines indicate Clausius – Clapeyron scaling rate. Note: Logarithmic vertical axis. Dataset used is IMD.